2014-04

Comparison of Methods for Extracting ADCIGS from RTM

UTD AUTHOR(S): Hu Jin and George A. McMechan

GEOPHYSICS, VOL. 79, NO. 3 (MAY-JUNE 2014); P. S89–S103, 16 FIGS., 1 TABLE.
10.1190/GEO2013-0336.1

Comparison of methods for extracting ADCIGs from RTM

Hu Jin[1], George A. McMechan[1], and Huimin Guan[2]

ABSTRACT

Methods for extracting angle-domain common-image gathers (ADCIGs) during 2D reverse-time migration fall into three main categories; direction-vector-based methods, local-plane-wave decomposition methods, and local-shift imaging condition methods. The direction-vector-based methods, which use either amplitude gradients or phase gradients, cannot handle overlapping events because of an assumption of one propagation direction per imaging point per imaging time; however, the ADCIGs from the direction-vector-based methods have the highest angle resolution. A new direction-vector-based method using instantaneous phase gradients in space and time gives the same propagation directions and ADCIGs as those obtained by the Poynting vector or polarization vector based methods, where amplitudes are large. Angles calculated by the phase gradients have larger uncertainties at smaller amplitudes, but they do not significantly degrade the ADCIGs because they contribute only small amplitudes. The local-plane-wave decomposition and local-shift imaging condition methods, implemented either by a Fourier transform or by a slant stack transform, can handle overlapping events, and produce very similar angle gathers. ADCIGs from both methods depend on the local window size in which the transforms are done. In small local windows, both methods produce ADCIGs with low noise, but also with low angle resolution; in large windows, they have high angle resolution, but contain smeared artifacts.

INTRODUCTION

A common-image gather (CIG) for a reflection point is a collection of prestack migrated traces at the same image location. Image traces that contribute to an output angle bin usually have different sources and receivers. CIGs are the primary data for amplitude-variation-with-offset (AVO) or amplitude-variation-with-reflection angle (AVA) analysis, and for migration velocity analysis (MVA). When a correct velocity model is used for migration, the events on a CIG are flat; the events are curved down when the migration velocities are higher than the correct velocities or curved up when the migration velocities are lower. The flatness of the events on CIGs is a principle criterion for updating the velocity model (by measuring the curvature of the CIG events), and for assessing quality of the velocity model. CIGs can be extracted as a function of surface attributes, such as surface offsets or as a function of subsurface attributes, such as subsurface offsets or reflection angles. CIGs sorted by the surface attributes suffer from migration artifacts that result from the multiple paths that occur in complicated structures (Nolan and Symes, 1996; Xu et al., 2001; Zhang et al., 2010). Xu et al. (2001) investigated the reasons for these artifacts using five surface attributes, and they show that an angle-domain common-image gather (ADCIG), in which the migrated contributions are sorted by reflection angle, reduces artifacts related to multipaths.

ADCIGs can be obtained by ray-based prestack migration, such as Kirchhoff depth migration (French, 1974; Gardner et al., 1974; Schneider, 1978), or beam migration (Hill, 2001; Gray, 2005), or by wave-equation based migration, such as one-way wave-equation migration (OWEM) (Biondi and Palacharla, 1996; Zhang et al., 2003), or reverse-time migration (RTM) (Chang and McMechan et al., 1986, 1990; Whitmore and lines, 1986). RTM, implemented by the two-way wave equation, provides the most accurate and complete images with the fewest assumptions compared with Kirchhoff depth migration (which is based on the high frequency approximation), beam migration (which is based on a Green's function approximation), or OWEM (which is based on the approximation of one-way propagation). The motivation described above for calculating ADCIGs from RTM is given in more detail by Zhang et al. (2010) and Xu et al. (2011).

There are three main methods for extracting ADCIGs from RTM; the direction-vector-based (DVB) methods, the local-plane-wave decomposition (LPWD) methods, and the local-shift image

Manuscript received by the Editor 4 September 2013; revised manuscript received 22 November 2013; published online 1 April 2014.
[1]The University of Texas at Dallas, Center for Lithospheric Studies, Richardson, Texas, USA. E-mail: hu.jin@utdallas.edu; mcmec@utdallas.edu.
[2]Total E&P Research and Technology, Houston, Texas, USA. E-mail: huimin.guan@total.com.

condition methods with subsurface-offset to angle transformation (e.g., Vyas et al., 2011a). Each of the three main methods can be implemented in various ways (Figure 1), each with its own accuracy, quality and performance.

DVB methods

The DVB methods include the Poynting-vector-based method (Yoon and Marfurt, 2006), the polarization-vector-based method (Zhang and McMechan, 2011a, 2011b), and the instantaneous-wavenumber vector-based method (Zhang and McMechan, 2011a, 2011b). These methods are fast and produce high angle resolution ADCIGs, but are not stable for complicated wavefields that contain overlapping events, because they calculate only one propagation direction per image point per time step (Vyas et al., 2011b). The algorithms in this category differ from each other either in the method of calculation of the reflection angle (from source and receiver wavefield propagation directions [Dickens and Winbow, 2011], or from source wavefield propagation directions and reflector dip angles [Zhang and McMechan, 2011a, 2011b; Yoon et al., 2011; Vyas et al., 2011b]), or in the amount of the data used (one, or a few, highest-amplitude arrivals [Zhang and McMechan, 2011a, 2011b; Yoon et al., 2011], or all arrivals at each grid point [Dickens and Winbow, 2011; Vyas et al., 2011b]).

LPWD methods by slant stacking or Fourier transforms

The LPWD methods decompose spherical wavefronts into locally planar waves. The propagation direction of each plane wave of the source and receiver wavefields can be calculated either by a slant stack (SS) transform (Xie and Yang, 2008a; Yan and Xie, 2011, 2012) or from the horizontal and vertical wavenumbers obtained by 2D Fourier transforming (FT) the local waves into the wavenumber domain (Xie and Wu, 2002; Xu et al., 2010b, 2011). These methods are more stable than the DVB methods in calculating the propagation angles, but are also more expensive (Xu et al., 2011; Yan and Xie, 2012). Choosing a local window size for the FT involves consideration of the trade-off between the angle resolution and the quality of the images (or the angle gather) (Xie and Wu, 2002; Yan and Xie, 2012).

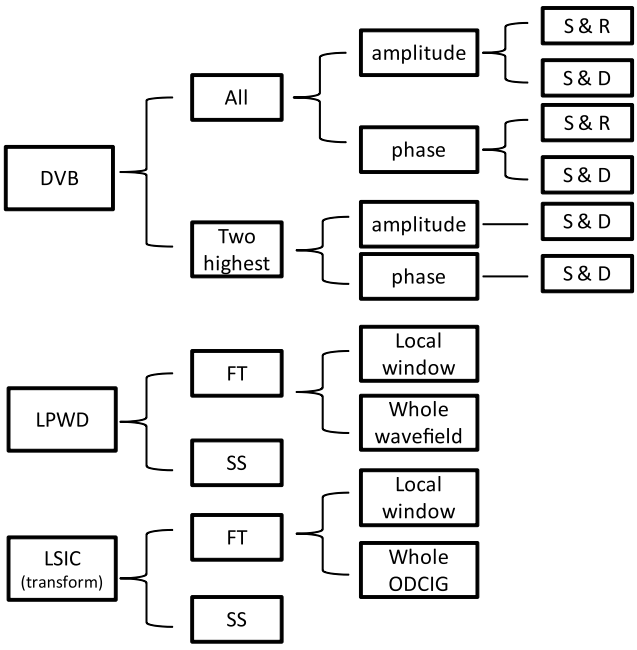

Figure 1. The relations between all the methods that are compared. "All" mean the full wavefields, and "two highest" mean the two highest amplitudes which are picked by scanning the wavefield over all time steps at each grid point. "Amplitude" means the amplitude-gradient method, and "phase" means the phase-gradient method. "S" means the source propagation angles, "R" means the receiver propagation angles, and "D" means the reflector dip angles.

Local-shift imaging condition methods by slant stacking or Fourier transforms

The local-shift imaging condition (LSIC) method is an indirect method for calculating the propagation directions from the source and receiver wavefields. It first produces subsurface-offset-domain common-image gathers (ODCIGs) by crosscorrelating the wavefields which are shifted horizontally and/or vertically with respect to each other, and then the ODCIGs are transformed into the ADCIGs. The transformation can be done either by 2D FTs (Sava and Fomel, 2003, 2005a, 2005b) or by an SS transform (Sava and Fomel, 2003; Biondi and Symes, 2004). Because the transformation is done only once for each CIG, the method is much faster than the LPWD methods (for 2D), but the ADCIGs often suffer from smearing-effect artifacts (Sava and Fomel, 2003; Dickens and Winbow, 2011; Xu et al., 2011).

There is another method, based on the time shift imaging condition (Sava and Fomel, 2006b), which is similar to the LSIC, but shifting is applied in the time domain between the source and receiver wavefields, rather than in the space domain. It first produces time-shifted CIGs by crosscorrelating the wavefields which are shifted in time with respect to each other, and then converts them into ADCIGs by slant stacking. The method is very efficient in 2D (Sava and Fomel, 2006b), but the angle resolution of the ADCIGs obtained from the method is lower than that from the local-shift (space domain) imaging condition (Sava and Fomel, 2006a), and cannot provide sufficient azimuthal information in 3D (Xu et al., 2011). Because of these limitations, the time-shift method is not as popular as the other methods, so we do not include it explicitly in this paper.

Previous comparisons of algorithms

Which method provides the best ADCIGs, considering the accuracy, the quality, and the cost? This is a critical question for later applications of the ADCIGs, which include wave-equation MVA (WEMVA) (Sava and Biondi, 2004; Sava and Vlad, 2008; Shen and Symes, 2008; Xie and Yang, 2008b; Zhang and Biondi, 2013), picking residual depth moveouts in CIGs for tomographic velocity updates (Siliqi et al., 2007; Siliqi and Talaalout, 2009; Liu and Han, 2010; Panizzardi et al., 2011), AVA analysis, or removing the low-wavenumber artifacts that appear mainly at shallow depths of individual and final stacked migrated images, generated from the crosscorrelation of reflections, head waves, diving waves, and backscattered waves (Baysal et al., 1984; Mulder and Plessix, 2003; Yoon et al., 2004; Yoon and Marfurt, 2006; Liu et al., 2007; Zhang and Sun, 2009; Zhang et al., 2010; Yan and Xie, 2009, 2010).

Partial comparisons of these methods have been made previously. Luo et al. (2010) compared the LPWD FT implementation and the LSIC SS implementation, using the parts of Sigsbee2A data set. Xu et al. (2011) compared ADCIGs obtained by an LPWD implemented by FT, and those obtained by an LSIC method, using the whole Sigsbee2A data set. Dickens and Winbow (2011) compared the ADCIGs obtained by the Poynting vector-based method and those obtained by the LSIC SS implementation, using parts of the SEAM subsalt model. Yoon et al. (2011) compared the ADCIGs obtained by the Poynting-vector-based method and those obtained by the LSIC method, using a narrow azimuth data set from 3D SEG/EAGE salt model. Zhang and McMechan (2011b) discuss the main differences between the polarization-vector-based method and LSIC method. Patrikeeva and Sava (2013) compared the cost and quality of the ADCIGs obtained by the LSIC method and the Poynting-vector-based method.

Each of the papers above compares only two methods, and the comparisons among them are somewhat inconclusive because the data sets are different, the parameters for the ADCIGs are different, and the pre- and postprocessing techniques are different. Here, we compare all the methods listed above using a single synthetic data set for a single model which allows comparative evaluation, and also reveals previously undiscussed relationships between the methods.

In the following sections, we first describe the test velocity model, the synthetic data generated from the model, preprocessing of the data, the imaging condition, and postprocessing of the ADCIGs. Then, in each of the three subsections of the Methods section, we describe the algorithms of each of the three main methods, and find the relationships, similarities, and differences between the different implementations of each (an "inner" comparison). In the next section, comparisons and discussions are done across the three main methods (an "outer" comparison).

TEST VELOCITY MODEL, SYNTHETIC DATA, PRE- AND POST-PROCESSING, AND IMAGING CONDITION

The velocity model used to generate the synthetic data contains a circular target (Figure 2), and two symmetric reflectors dipping at 30°. The reason for choosing the circular target is that it contains all dips and all possible wavenumbers, and that it generates complicated data, such as overlapping events, multipaths, diffractions, and reflected waves (Figure 3a).

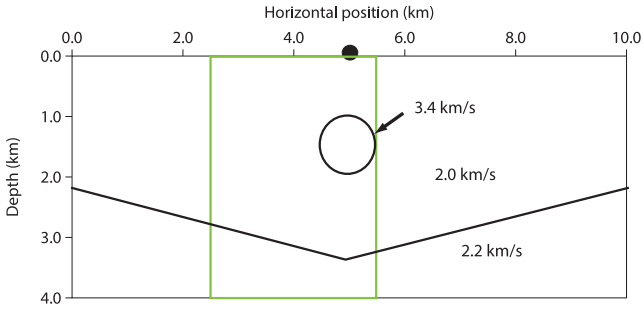

Figure 2. The velocity model used to produce the synthetic data. The black dot represents a source at the middle of the surface, at the horizontal position of 5.0 km. The green box, from 2.5 to 5.5 km, shows the area in which ADCIGs are displayed in later figures. The recorded data from the receivers outside of the green box are needed to provide complete angle gather information inside the box.

A 2D scalar finite-difference extrapolator that is eighth-order in space and second-order in time is used to generate the data. The grid increment in the vertical and the horizontal dimensions is 10 m and the time sample increment is 1 ms. The explosive source has a Ricker wavelet with 20 Hz dominant frequency and bandwidth from 0.0 to 65.0 Hz. A total of 250 sources are located at the top of the model between horizontal positions of 2.5 and 7.5 km with an interval of 20 m, and there is a total of 500 receivers extending across the entire surface of the model with an interval of 20 m. All the receivers are active for each source. Because the model is symmetric around the center position at 5.0 km, below we display the ADCIGs only within the green box marked in Figure 2. Preprocessing applied to the recorded common-source gathers include direct wave removal and tapering at their left and right edges. Postprocessing involves a median filter applied to each ADCIG. The ADCIGs have angle bins of 1° for all methods.

Instead of saving the source time snapshots for all the time steps for the crosscorrelation image condition, we use the snapshots only at every eighth time step, which satisfies the Nyquist sampling requirement up to 60 Hz (Sun and Fu, 2013)

$$f_s \geq 2f_c, \quad 1/(8 * dt) = 125 \text{ Hz} > 2 \times 60 \text{ Hz}, \tag{1}$$

where f_s is the sampling frequency, and f_c is the highest frequency in the data. Saving snapshots at every eighth time step neither introduces grid dispersion nor affects the stability condition because subsequent resampling in time does not change the space or time increment used in the source and receiver wavefield extrapolations.

The prestack migrated image for each source is obtained using the crosscorrelation imaging condition,

$$\mathbf{I}(\mathbf{x}) = \sum_s \left(\sum_t \right) \mathbf{U_s}(\mathbf{x}, t)\mathbf{U_r}(\mathbf{x}, t), \tag{2}$$

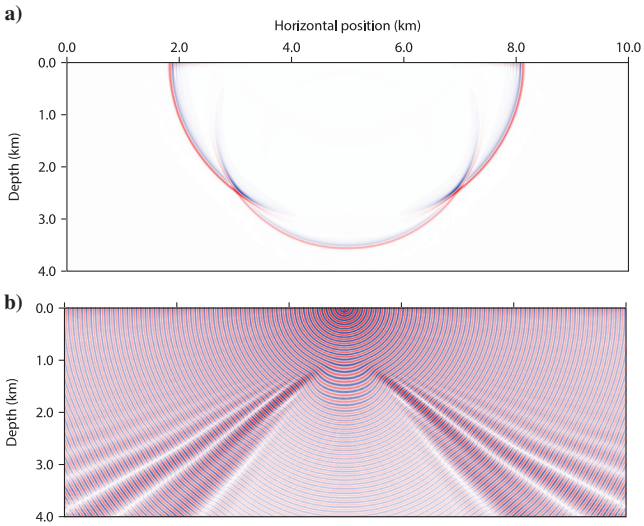

Figure 3. Source wavefields generated from the source marked in Figure 2; (a) is in the time domain at a time of 1.6 s, and (b) is the 25 Hz frequency component of (a).

in the time (t) domain, or

$$\mathbf{I}(\mathbf{x}) = \sum_s \left(\sum_\omega \mathbf{U_s}(\mathbf{x}, \omega) \mathbf{U_r^*}(\mathbf{x}, \omega) \right), \tag{3}$$

in the frequency (ω) domain. Here, s is the source index, r is the receiver index, $\mathbf{x}$ is the spatial location, and $\mathbf{I}$ is the stacked RTM image. The images are migrated with a smoothed version of the correct velocity model. The crosscorrelation image can be normalized by the square of the source strength (Kaelin and Guitton, 2006; Chattopadhyay and McMechan, 2008), but this source-normalization is not applied to any of the ADCIGs in this paper because most of the previous papers do not use the source-normalized crosscorrelation imaging condition (Yan and Sava, 2008; Xu et al., 2011; Yoon et al., 2011; Zhang and McMechan, 2011b; Yan and Xie, 2012).

The source and receiver wavefields $\mathbf{U_s}(\mathbf{x}, t)]$ and $\mathbf{U_r}(\mathbf{x}, t)]$ in the space/time domain, are computed by time stepping with a 2D scalar eighth-order finite-difference extrapolator. The source and receiver wavefields $\mathbf{U_s}(\mathbf{x}, \omega)]$ and $\mathbf{U_r}(\mathbf{x}, \omega)]$ in the space/frequency domain are computed by 1D Fourier transforming $\mathbf{U_s}(\mathbf{x}, t)$ and $\mathbf{U_r}(\mathbf{x}, t)$, respectively,

$$\mathbf{U_s}(\mathbf{x}, \omega) = \sum_t \left(\mathbf{U_s}(\mathbf{x}, t) e^{-i\omega t} \right), \tag{4a}$$

and

$$\mathbf{U_r}(\mathbf{x}, \omega) = \sum_t \left(\mathbf{U_r}(\mathbf{x}, t) e^{-i\omega t} \right), \tag{4b}$$

although they are normally computed by a 2D frequency domain extrapolator using direct LU solvers (Pratt, 1990; Xu et al., 2010a). All of the DVB methods use the time domain imaging condition 2. The LPWD and LSIC methods use the frequency domain imaging condition 3. Figure 4 contains an example of the RTM image for a single source located at the middle of the upper surface (the dot at 5.0 km in Figure 2), using the crosscorrelation imaging condition. Note that the images contain many artifacts, some of which (e.g., events 6 and 7) can be reduced by using a more-highly-smoothed migration velocity model in RTM.

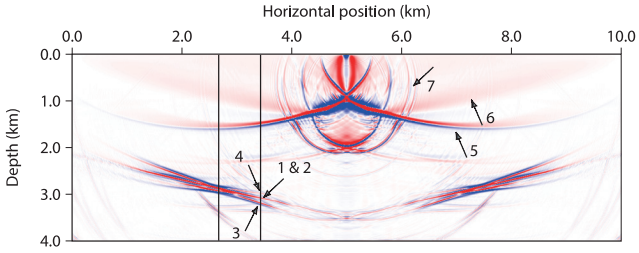

Figure 4. The RTM image from a single source located at 5.0 km, obtained by using equation 2. The two black vertical lines at 2.6 and 3.3 km are the positions where the single ADCIGs in Figure 13a–13e are extracted. Events 3 and 4 are the RTM artifacts that result from crosscorrelation of diffracted and reflected waves (see the source wavefield in Figure 3). Events 1 and 2 are reflection points with different reflection angles (see Figure 13). Event 5 is an artifact, from crosscorrelation between the source wavefield and the reconstructed receiver wavefield, which may be reduced by applying stronger taper at the edges of the common-source gathers. Event 6 is a low-wavenumber artifact (Zhang and Sun, 2009), and event 7 is an artifact from internal reverberation inside the circular target.

METHODS

This section is divided into three subsections. The first contains the DVB methods, the second contains the local-plane-wave decomposition methods, and the third contains the local-shift methods.

The DVB methods

In this category, various methods have been proposed, all of which can be differentiated mainly by three factors: (1) three different methods to calculate propagation angles, (2) two different strategies to calculate incident/reflection angles, and (3) the amount of data used. Each factor is compared in turn.

Calculating the source and receiver propagation angles

The source and receiver propagation angles can be computed by the Poynting-vector-based method, the polarization-vector-based method (which calculate the first spatial derivatives of amplitudes), and the instantaneous-wavenumber-vector-based method (which calculates the first spatial derivatives of instantaneous phase).

The Poynting vector can be used to calculate propagation directions (Yoon et al., 2004). The 2D Poynting vector is

$$\nabla \mathbf{U} \cdot \frac{\partial \mathbf{U}}{\partial t} = \left(\frac{\partial \mathbf{U}}{\partial x}, \frac{\partial \mathbf{U}}{\partial z} \right) \cdot \frac{\partial \mathbf{U}}{\partial t}, \tag{5}$$

where $\mathbf{U}$ is either the source wavefield or the receiver wavefield, t is time, and x and z are the horizontal and the vertical coordinates, respectively. Zhang and McMechan (2011b) have proposed a method to calculate propagation directions based on the physical property that P-wave propagation direction is parallel to the polarization direction of the P-wave displacement (the polarization-vector-based method) in isotropic media and is written as

$$\nabla \mathbf{U} = \left(\frac{\partial \mathbf{U}}{\partial x}, \frac{\partial \mathbf{U}}{\partial z} \right). \tag{6}$$

In anisotropic media, they are not necessarily parallel (Zhang and McMechan, 2011a). Although equation 6 is derived and explained physically, the polarization-vector-based method is similar to equation 5 of the Poynting-vector-based method. The time derivative in equation 5 corrects for the polarity changes in alternate half cycles to give a consistent estimate of the propagation direction (Figure 5a and 5b). When the time derivative is positive, two methods give the same propagation directions, but when the time derivative is negative, two methods give the opposite propagation directions. Because the Poynting vector-based method and the polarization-based method are based on the amplitude gradients and provide the same (or opposite) directions, they are considered as the same (amplitude-gradient) method in this paper (Figure 5a and 5b). The reference direction for the propagation angle is vertically downward and the sign of all angles is positive counterclockwise.

An alternate method uses instantaneous wavenumber (Havlicek et al., 1998). Zhang and McMechan (2011b) applied it to a stacked migrated image to calculate reflector dips. As one of the DVB

methods, this is also based on the first spatial derivatives, but uses the instantaneous phases of the wavefields in the space domain, instead of the amplitudes. The instantaneous phase of a 2D wavefield may be computed by either one of two 1D directional Hilbert transforms (Havlicek et al., 1998); H_1 over the horizontal direction,

$$\mathbf{q}_1(x,z) = H_1[\mathbf{U}(x,z)] = \frac{1}{\pi}\int_{\mathbf{R}} \mathbf{U}(x-\xi,z)\frac{d\xi}{\xi}, \quad (7)$$

or H_2 over the vertical direction,

$$\mathbf{q}_2(x,z) = H_2[\mathbf{U}(x,z)] = \frac{1}{\pi}\int_{\mathbf{R}} \mathbf{U}(x,z-\eta)\frac{d\eta}{\eta}, \quad (8)$$

where ξ and η are dummy variables of integration, and $\mathbf{q}(x,z)$ is the Hilbert transformed (imaginary) wavefield, which varies with spatial position. The instantaneous phase (by definition) is

$$\varphi(x,z) = \arctan\ \frac{\mathbf{q}(x,z)}{\mathbf{U}(x,z)}, \quad (9)$$

where the arctangent is implemented using the intrinsic function ATAN2 to go smoothly through the singularities where $\mathbf{U}(x,z) = 0$ at $\varphi(x,z) = \pm\pi/2$. Figure 5c shows $\varphi_2(x,z)$ calculated from the snapshot in Figure 3a using the vertical Hilbert transform H_2.

Havlicek et al. (1998) show that the first spatial derivatives of the instantaneous phase give components of the phase gradient,

$$\nabla\varphi(x,z) = \frac{\partial\varphi}{\partial x}, \frac{\partial\varphi}{\partial z}. \quad (10)$$

Here, $\nabla\varphi(x,z)$ is orthogonal to the local wavefield orientation (opposite to, or in the same direction as, the propagation) (see Appendix A).

Depending on the direction that the 1D Hilbert transform is taken over the 2D wavefields, $\mathbf{q}_1$ and $\mathbf{q}_2$, and corresponding $\nabla\varphi_1$ and $\nabla\varphi_2$ are different (Havlicek et al., 1998) (see Appendix A). However, by multiplying the spatial derivatives of the phase by the first time derivative of the phase,

$$\nabla\varphi(x,z)\cdot\frac{\partial\varphi}{\partial t} = \frac{\partial\varphi}{\partial x}, \frac{\partial\varphi}{\partial z}\cdot\frac{\partial\varphi}{\partial t}, \quad (11)$$

where $\nabla\varphi_1\cdot\frac{\partial\varphi_1}{\partial t}$ and $\nabla\varphi_2\cdot\frac{\partial\varphi_2}{\partial t}$ provide the same propagation directions (see Appendix A). Figure 5d shows the propagation directions calculated by $\nabla\varphi_2\cdot\frac{\partial\varphi_2}{\partial t}$. We call equations 10 and 11 phase-gradient methods.

To reduce ambiguity in the Poynting vectors when crossing a peak or a trough of the wavefields (where the derivatives are zero), three methods have been proposed for the amplitude-gradient method; averaging the Poynting vectors in space over four time periods of the source wavelet (Yoon et al., 2011), a least squares solution over a time window (Yan and Ross, 2013), or smoothing the Poynting vectors in the space domain (Dickens and Winbow, 2011). We find these also stabilize the phase-gradient calculations. In Figure 5b and 5d, and in all the examples below, we use a median filter of the propagation directions in the space domain.

Which method gives the more accurate and robust estimates of the propagation direction; the amplitude-gradient (equation 5) or the phase-gradient (equation 11)? There are no quantitative calculations available to compare to for complicated wavefields (Luo et al., 2010), but a qualitative evaluation can be made based on the fact that the propagation direction is perpendicular to the local plane wave. To make the comparison, we consider the LPWD method which should be more accurate for complicated wavefields (Xie and Wu, 2002; Xu et al., 2011) (described in detail in the next section) to evaluate the directions computed with the amplitude-gradient and the phase-gradient methods.

Figure 6b shows propagation directions estimated from the amplitude and phase gradients (the blue and red arrows, respectively) at four representative points (the black dots) corresponding to high amplitudes. Where only one wavefront is present in a calculation window, these and the results of the LPWD method (the black arrows) are nearly coincident (Figure 6b). Where two wavefronts exist in the domain of the calculations (in the box, Figure 6b), the LPWD method provides estimated directions for both wavefronts (the black and green arrows) but the DVB methods (the red and blue arrows) both give similar, single estimates (Figure 6b) that are weighted propagation directions (Patrikeeva and Sava, 2013). This is the main limitation of the DVB methods, and is a consequence of the assumption that there is only one direction per image point per image time (Vyas et al., 2011b).

Figure 6c shows estimated propagation directions at four representative points (the green dots) corresponding to low-amplitude wavefront points. The differences in the propagation directions estimated from the amplitude and phase gradients (Figure 6a) are

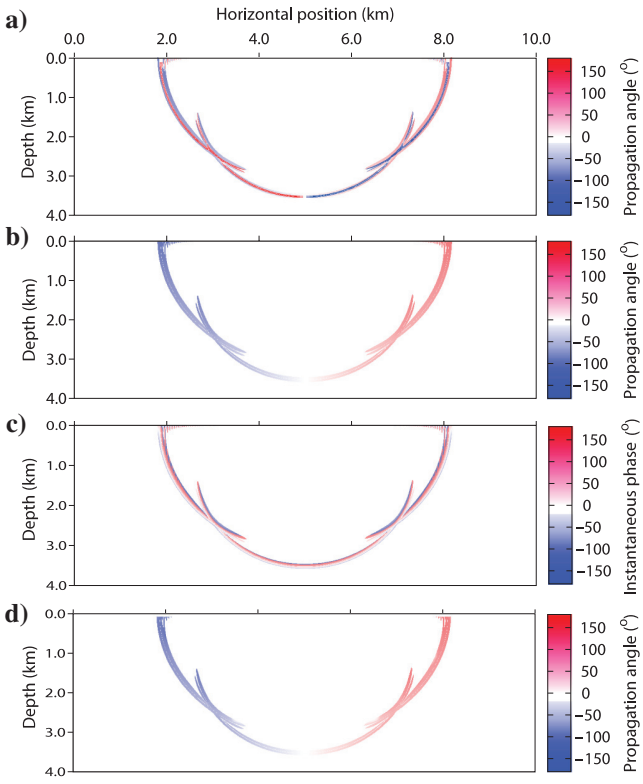

Figure 5. The propagation angles calculated (a) with equation 6, (b) with equation 5. (c) The instantaneous phase computed from equation 9, and (d) the propagation angle calculated with equation 11. A median filter is applied to the computed propagation angles.

higher at the low-amplitude points (Figure 6c) than at the high-amplitude points (Figure 6b), and the amplitude-gradient results match better with the LPWD results at low-amplitude points (Figure 6c). Random noise increasingly contaminates the phase estimates as the signal amplitude decreases. In the limit where only random noise is present, the phase estimates will also be random, but this has negligible effect on the ADCIG when the signal amplitude is small. So we conclude that the amplitude gradient and phase gradient results are similar, qualitatively accurate, and match well with the LPWD results, except where more than one wavefront exists in the local area of the calculation (Figure 6b), or where the signal amplitudes are low (Figure 6c).

Calculating incident/reflection angles

As part of the crosscorrelation imaging condition applied at each time step, the reflection angle (or incident angle) is computed at each grid point. This can be written as

$$\mathbf{I}(\mathbf{x},\theta)=\sum_s\left(\sum_t\right)\mathbf{U_s}(\mathbf{x},\theta_s,t)\mathbf{U_r}(\mathbf{x},\theta_r,t), \tag{12}$$

where each reflection angle θ, is computed from a source propagation angle θ_s, and a receiver propagation angle θ_r,

$$\theta=(\theta_s-\theta_r)/2. \tag{13}$$

θ_s and θ_r can be calculated either by the amplitude-gradient or the phase-gradient method. Alternatively, the reflection angle can also be computed from a source propagation angle and a reflector dip angle θ_d, which is calculated from the stacked migrated image (Zhang and McMechan, 2011a),

$$\theta=\theta_s-\theta_d. \tag{14}$$

The crosscorrelation imaging condition can be rewritten as

$$\mathbf{I}(\mathbf{x},\theta)=\sum_s\left(\sum_t\right)\mathbf{U_s}(\mathbf{x},\theta_s,t)\mathbf{U_r}(\mathbf{x},t). \tag{15}$$

The algorithm that calculates reflection angles from the source propagation angles θ_s, and reflector dip angles θ_d takes about half of the computation time of that based on the source and receiver propagation angles. This is because the reflector dip angles is calculated only once for the stacked migrated image, whereas the receiver propagation angles need to be calculated repetitively in the source and time loops.

The ADCIGs obtained from the amplitude-gradient methods (Figure 7a and 7c) and those obtained from the phase-gradient methods (Figure 7b and 7d) are very similar, which is expected because the propagation directions calculated by these two methods are very similar (except where the amplitudes are very low). The ADCIGs obtained from the source propagation angles and the reflector dip angles (Figure 7c and 7d) are not as coherent in the subsalt areas than those obtained from the source and the receiver propagation angles (Figure 7a and 7b). This may result from inaccurate estimates of the reflector dip angles that are calculated by the phase-gradient method (Zhang and McMechan, 2011b), which are unreliable at the very-low-amplitude points in the subtarget areas where there is low illumination. The reflector dips can be calculated more accurately by LPWD (Vyas et al., 2011b), which is more expensive than the phase-gradient method.

The ADCIGs obtained from the source and the receiver propagation angles may be noisier and less reliable than those obtained from the source propagation angles and the reflector dip angles, in more complicated synthetic models or for real data because the receiver wavefield is often more complicated (with more overlapping events) and noisier than a stacked migrated image (Vyas et al., 2011b; Yoon et al., 2011; Zhang and McMechan, 2011b).

The amount of data used

Yoon et al. (2011) and Zhang and McMechan (2011b) improve the efficiency by calculating the propagation angles, by the amplitude-gradient method (equations 5 and 6, respectively), only at the times (excitation times) when a few highest amplitude arrivals of the source wavefield occur at each grid point, rather than calculating angles at all time steps (all arrivals) and at each grid point as in the crosscorrelation method.

Figure 8a and 8c show the propagation angles of the highest and second highest amplitude arrivals computed by the amplitude-gradient method (equation 5) at all grid points, and Figure 8b and 8d show the propagation angles of the highest and second highest amplitude arrivals computed by the phase-gradient method (equation 11). These two methods show the same angle estimates everywhere, for both arrivals, as a consequence of the use of only high-amplitude arrivals, and of the median filter applied to the angle estimates. Consequently, the ADCIGs obtained from the amplitude and phase-gradient methods (Figure 9a and 9b, respectively) are virtually identical to each other, and to those obtained using all

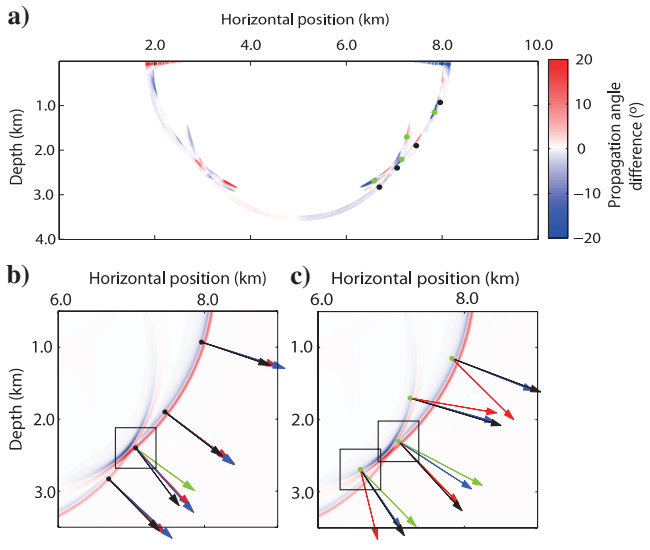

Figure 6. (a) The differences between the propagation angles calculated using the amplitude-gradient and the phase-gradient methods, for the wavefield in Figure 3a. (b) The propagation directions estimated from the amplitude (the blue arrows) and the phase gradients (the red arrows) are similar at four representative high amplitude points (the black dots in [a]), but (c) they are different at four representative low amplitude points (the green dots in [a]). In (b and c), the black and green vectors represent the propagation directions calculated by the LPWD method, and correspond to two plane waves in each of the local windows.

arrivals in Figure 7c and 7d. We conclude that most of the useful information in this example is contained in the two highest amplitude arrivals.

The LPWD methods

The LPWD methods assume that a spherical wavefront is the superposition of local plane waves, each with their own wavenumber. Thus, a decomposition is implemented by applying either an FT or an SS transform to the plane waves in local windows, or over the whole wavefield.

The LPWDs have been implemented by applying FTs in local windows (Xie and Wu, 2002; Xu et al., 2011). Following Xu et al. (2011), the source $\mathbf{U_s}(\mathbf{x},\omega)]$ (equation 4a) and receiver $\mathbf{U_r}(\mathbf{x},\omega)]$ (equation 4b) wavefields in the space/frequency domain are first transformed into the wavenumber/frequency domain, $\mathbf{U_s}(\mathbf{k},\omega)]$ and $\mathbf{U_r}(\mathbf{k},\omega)$,

$$\mathbf{U_s}(\mathbf{k_s},\omega) = \sum_{\mathbf{x}} \mathbf{U_s}(\mathbf{x},\omega) e^{-i\mathbf{k_s}\mathbf{x}}, \tag{16a}$$

and

$$\mathbf{U_r}(\mathbf{k_r},\omega) = \sum_{\mathbf{x}} \mathbf{U_r}(\mathbf{x},\omega) e^{-i\mathbf{k_r}\mathbf{x}}. \tag{16b}$$

Then, a reflection angle is calculated from the wavenumbers of the forward propagating source and receiver wavefields, $\mathbf{k_s}$ and $\mathbf{k_r}$.

$$\cos\theta = \frac{\mathbf{k}\cdot\mathbf{k_r}}{|\mathbf{k}||\mathbf{k_r}|}, \tag{17}$$

where $\mathbf{k}$ is a vector wavenumber of an imaged locally planar reflector, expressed as $\mathbf{k} = \mathbf{k_s} + \mathbf{k_r}$ (Xu et al., 2011).

Finally, the crosscorrelation imaging condition is applied with reflection angle θ in the frequency/wavenumber domain (Xu et al., 2011),

$$\mathbf{I}(\mathbf{k},\theta) = \sum_{\omega} \left(\sum_{\mathbf{k_s}-\mathbf{k_r}} \delta(\theta-\theta_0)\mathbf{U_s}(\mathbf{k_s},\omega)\mathbf{U_r}(\mathbf{k_r},\omega), \right. \tag{18}$$

which is inverted into the spatial domain by a 2D inverse FT (for 2D data),

$$\mathbf{I}(\mathbf{x},\theta) = \sum_{\mathbf{k}} \mathbf{I}(\mathbf{k},\theta) e^{i\mathbf{k}\mathbf{x}}, \tag{19}$$

where θ_0 is a reference direction, which is vertically downward.

The wavenumber/frequency domain product in equation 18 represents a 2D wavenumber convolution of the source and receiver wavefields (Xu et al., 2011), so it is very expensive. To reduce the cost, Xu et al. (2011) developed an antileakage Fourier transform (ALFT) (Xu et al., 2005, 2010b) to use only the most energetic

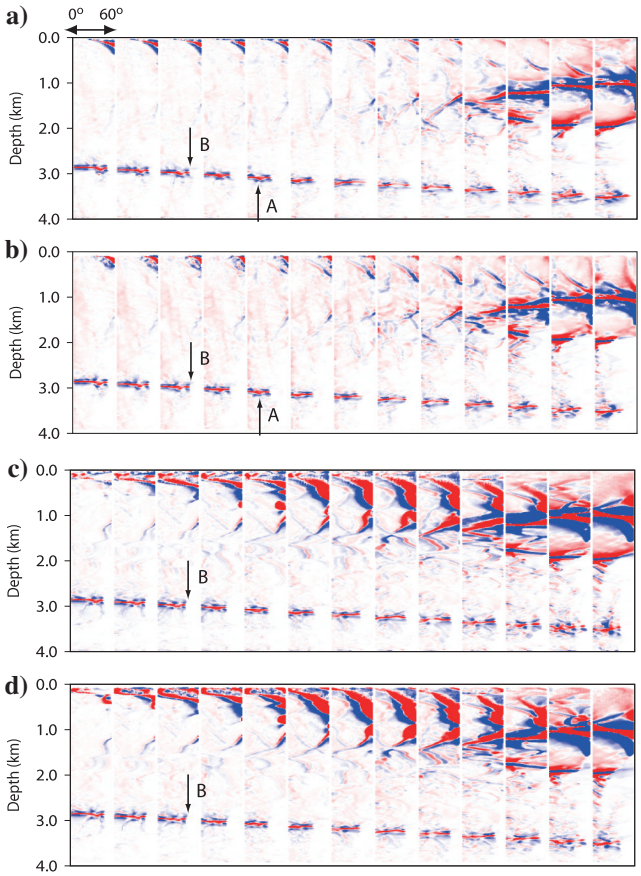

Figure 7. ADCIGs obtained using the source and receiver propagation angles by (a) the amplitude-gradient method, and by (b) the phase-gradient method. ADCIGs obtained using the source propagation angles and the reflector dip angles by (c) the amplitude-gradient method, and (d) the phase-gradient method. The horizontal ranges of the ADCIGs are shown in the green box in Figure 2. The event A is explained in Figure 13, and the event B is explained in the text.

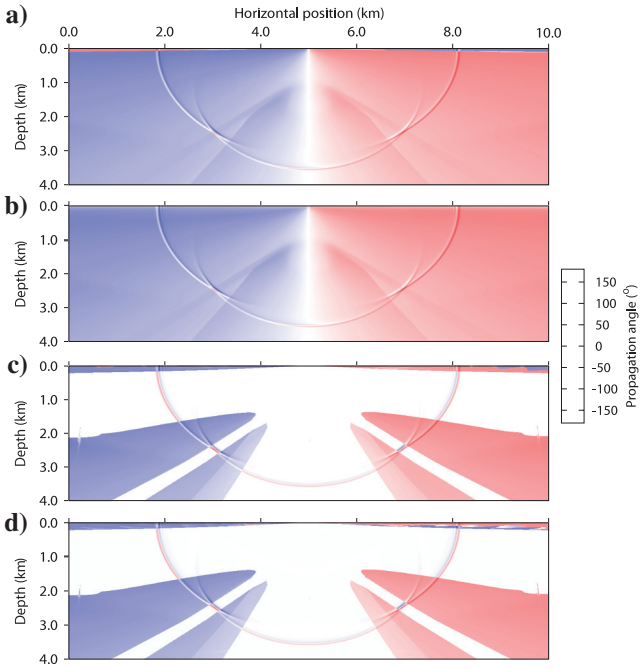

Figure 8. The propagation angles of the highest amplitude arrivals are calculated by (a) the amplitude-gradient method, and (b) the phase-gradient method. The propagation angles of the second-highest amplitude arrivals are calculated by (c) the amplitude-gradient method, and (d) the phase-gradient method. The wavefront overlain on the propagation angles is the snapshot in Figure 3a.

wavenumbers (where "energy" is defined as the spectral power at each location in the wavenumber/frequency domain). Here, we take ~900 wavenumbers with the highest spectral powers from a total of 256 × 256 wavenumbers (after applying zero-padding to the input data) by using the ALFT in each window (Figure 10a).

The LPWD method can be implemented by using local windows in the source and receiver wavefields in the space/frequency domain, which gives good local approximations of the plane waves. The method also can be implemented by transforming whole source and receiver wavefields from the space/frequency domain to the wavenumber/frequency domain. However, the convolution (equation 18) in the wavenumber/frequency domain using the whole wavefield (even for 2D data) is so expensive that it is not practical in present-day supercomputers (Xu et al., 2011).

The ALFT works well for local windows, but is not efficient for the whole wavefield (i.e., for very large windows) because large windows contain many different energetic wavenumbers (local plane waves), each of which needs to be inverse transformed separately (Xu et al., 2011). Thus, to make the process practical, and to find the most energetic wavenumbers efficiently, we set a threshold (a minimum energy) for each wavefield in the frequency/wavenumber domain, and use only the wavenumbers whose energies are larger than the threshold. For example, here, the threshold is set as 10% of the highest energy in each wavefield in the wavenumber domain. There is a trade-off in choosing a threshold between the cost and the proportion of the image recovered by the inverse 2D FT. If the threshold is set higher, fewer wavenumbers are included, so the computational cost will be reduced, but the images of the low-amplitude (energy) contributions will not be well recovered, such as in the subtarget area in the green oval in Figure 10b. On the other hand, if the threshold is smaller, more wavenumbers are taken; thus, the small amplitude images may be recovered, but the computation cost will be increased.

When determining a local window size, there is another trade-off between reducing the quality (in the form of smearing-effect artifacts) and reducing the angle resolution in the ADCIGs. A small window is more likely to satisfy the local-plane-wave assumption, so the resulting ADCIGs are relatively clean, but the angle resolution is poor (Figure 10a). A large window does not always satisfy the local-plane-wave assumption, so the resulting ADCIGs can be very noisy, including the curved smearing-effect artifacts (see the blue ovals in Figure 10b) resulting from Fourier transforming nonplanar-waves. However, the local window size does not affect spatial resolution because the Fourier transform is invertible. The wavefield in each window can be transformed back to the original wavefield in the space/frequency domain, after the propagation angles are calculated in the wavenumber/frequency domain.

The LPWD method may also be implemented by calculating the propagation directions of local plane waves with an SS transform in the space/time domain (Yan and Xie, 2009, 2010), or in the space/frequency domain (Yan and Xie, 2011). The implementation in the space/frequency domain can be written as (Yan and Xie, 2011),

$$\mathbf{U}(\mathbf{x_0}, \omega, \theta_s/\theta_r) = \sum_{\mathbf{x}} \mathbf{U}(\mathbf{x}, \omega) e^{i\omega \mathbf{p}(\mathbf{x}-\mathbf{x_0})}, \qquad (20)$$

where $\mathbf{x_0}$ is the center position of the local window, and $\mathbf{V}$ and $\mathbf{p} = 1/\mathbf{V}$ are the velocity vector and the slowness vector in the propagation direction, respectively. Equation 20 calculates a stacked amplitude along a propagation angle θ_s or θ_r, through a reference point $\mathbf{x_0}$. Equation 20 needs to be computed iteratively in a loop over all propagation angles θ_s or θ_r, at each grid point. What is different from the conventional SS is that equation 20 not only stacks the amplitudes along the search lines, but stacks all the amplitudes at the grid points in the window along direction $\mathbf{p}$. The dot product of position $(\mathbf{x_0} - \mathbf{x})$, with the search propagation direction $\mathbf{p}$, determines the weight of the amplitude at each grid point to be stacked. So, when the angle α between vectors $\mathbf{p}$ and $(\mathbf{x_0} - \mathbf{x})$] is 90°, the weight will be maximum, and therefore the stacked

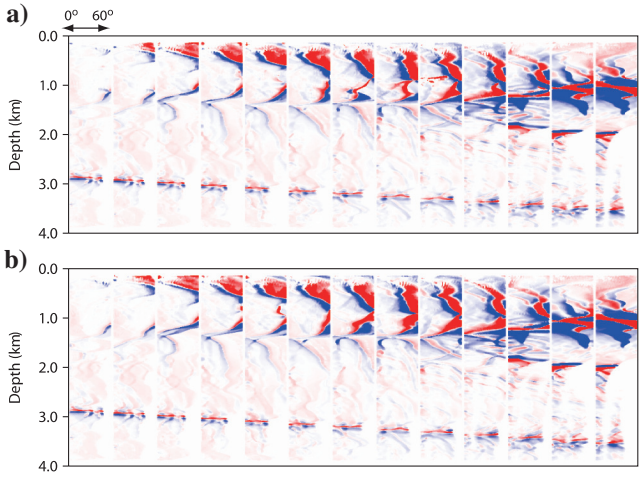

Figure 9. The ADCIGs obtained for the two highest-amplitude arrivals using (a) the amplitude-gradient method, and (b) the phase-gradient method. The horizontal ranges of (a and b) coincide with the green box in Figure 2.

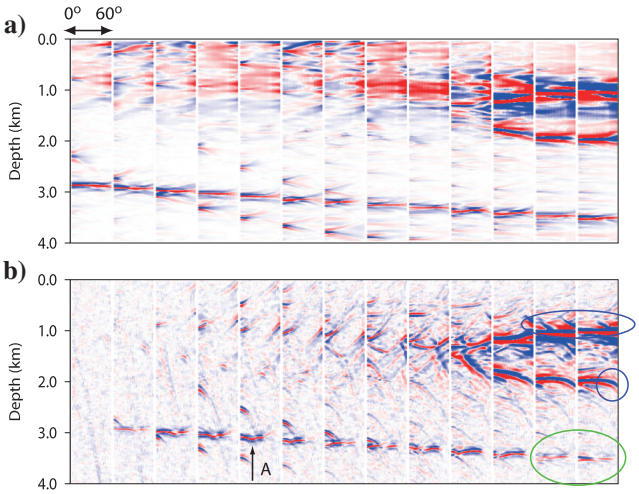

Figure 10. (a) The ADCIGs obtained from the LPWD method with the window size of 32 × 32 grid points. To remove wraparound and Gibbs artifacts, and to increase the wavenumber sampling, each window is extended into the size of 256 × 256 grid points by zero-padding. (b) The ADCIGs obtained from the LPWD method by transforming the whole source and receiver wavefields (e.g., very large window) have low illumination at subsalt reflector because we use only the most energetic wavenumbers, to reduce the computational time. The horizontal ranges of the ADCIGs coincide with the green box in Figure 2. The event A is explained in Figure 13. The events in the blue ovals are smearing-effect artifacts, and the green oval is explained in the text.

amplitude will be highest when the propagation direction is perpendicular to the plane wave;

$$(\mathbf{x}-\mathbf{x_0})\cdot\mathbf{p}=\|\mathbf{x}-\mathbf{x_0}\|\|\mathbf{p}\|\cos\alpha. \tag{21}$$

Note that equation 20 is expressed as an FT over $\mathbf{x_0}$.

Is there any relationship between the LPWD methods with SS transform and FT? To answer this question, replace $\omega\mathbf{p}$ with $\mathbf{k_p}$ in equation 20,

$$\mathbf{U}(\mathbf{x_0},\omega,\theta_s/\theta_r)=\sum_{\mathbf{x}}\mathbf{U}(\mathbf{x},\omega)e^{-i\mathbf{k_p}\mathbf{x}}e^{i\mathbf{k_p}\mathbf{x_0}}. \tag{22a}$$

Evaluating the FT over x gives

$$=\mathbf{U}(\mathbf{k_p},\omega)e^{i\mathbf{k_p}\mathbf{x_0}}, \tag{22b}$$

or

$$=\mathbf{U}(\mathbf{k_p},\omega,\theta_s/\theta_r)e^{i\mathbf{k_p}\mathbf{x_0}}, \tag{22c}$$

which a special case of equation 16b with an FT by considering only the center point $\mathbf{x_0}$, and a wavenumber $\mathbf{k_p}$ with a propagation direction θ_s or θ_r. Therefore, the FT and the SS methods (in the frequency domain) can be considered the same, even though they are explained differently in their respective domains. Detailed comparisons of the advantages and disavantages between the LPWD method by FT and the LPWD method by SS are discussed by Yan and Xie (2012).

LSIC methods

The LSIC method is an indirect method to extract ADCIGs from RTM. The method first generates subsurface-offset-domain CIGs (ODCIGs) by crosscorrelating source and receiver wavefields (e.g., Figure 3b), that are shifted relative to each other in the space/frequency domain (Sava and Fomel, 2003, 2005a, 2005b; Biondi and Symes, 2004), expressed as

$$\mathbf{I}(\mathbf{x},\mathbf{h})=\sum_{s}\left(\sum_{\omega}\mathbf{U_s}(\mathbf{x}-\mathbf{h},\omega)\mathbf{U_r^*}(\mathbf{x}+\mathbf{h},\omega)\right), \tag{23}$$

where $\mathbf{h}=(h_x,h_z)$ is a shift vector, in the x and z space coordinates, and * represents the conjugate of a complex value. Then, the ODCIGs are transformed into ADCIGs by an SS transform (Ottolini, 1982; Sava and Fomel, 2003) or an FT (Sava and Fomel, 2005a, 2005b) which is applied independently to each ODCIG based on the local-plane-wave assumption that a spherical wavefield is composed of locally planar waves. In this example, for common-source data generated from the velocity model in Figure 2, we shift the source and receiver wavefields in the space/frequency domain horizontally $\mathbf{h}=(h_x,h_z=0)]$ to get the horizontal-subsurface-offset-domain CIGs (HOCIGs) (Figure 11),

$$\mathbf{I}(x,z,h_x)=\sum_{s}\left(\sum_{\omega}\mathbf{U_s}(x-h_x,z,\omega)\mathbf{U_r^*}(x+h_x,z,\omega)\right). \tag{24}$$

HOCIGs become unsuccessful as the reflection dip increases (Biondi and Symes, 2004). So, to handle data from a complicated velocity model, which includes arbitrary reflector dips, HOCIGs and vertical-subsurface-offset-domain CIGs (VOCIGs) may need to be considered (Biondi and Symes, 2004; Shan and Biondi, 2008). A 2D FT is applied to each HOCIG, and reflection angles are then calculated for each combination of depth wavenumber k_z, and horizontal-offset wavenumber k_{h_x} using

$$\tan\theta=\frac{k_{h_x}}{k_z}. \tag{25}$$

The main idea and the procedure of transforming HOCIGs into ADCIGs by FT are the same as those used for the LPWD methods to calculate the propagation angles by an FT. So, the transformation again can be done within local windows, or over each complete HOCIG (Figure 12a and 12b, respectively). Interestingly, the ADCIGs obtained by the LSIC methods are very similar to those obtained by the LPWD methods using small local windows (compare Figures 10a and 12a), or transforming the whole wavefield or HOCIG (compare Figures 10b and 12b). The ADCIGs obtained from both methods depend on the size of the window used. The LSIC using an SS (Figure 12c) is not accurate in terms of amplitude or phase; the original waveforms are altered (Luo et al., 2010).

COMPARISONS AND DISCUSSION

In this section, we evaluate and compare the results of each of three main methods of extracting ADCIGs from RTM (Figure 1). The algorithms differ mainly in their implementations, whereas the principles remain the same.

The DVB and the LPWD methods are direct methods for extracting ADCIGs, whereas the LSIC method is an indirect method, involving an intermediate step of calculating HOCIGs. The DVB methods are implemented in the time domain, the LPWD method is implemented in the frequency domain, and the LSIC method can be implemented in either the time or frequency domain.

All the DVB methods are based on the assumption that there is one wave propagation direction per image point per image time, so the calculated propagation angles at points where there are overlapping events are unreliable (Figure 6b and 6c), and the corresponding amplitude from the overlapping events are also unreliable (e.g., the upper panel of Figure 13a); the largest CIG amplitudes (at the reflection angle estimated by DVB) lie between, rather than at, the two events 1 and 2. This is because the propagation angle calculated

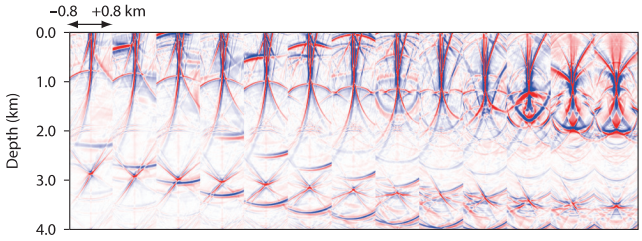

Figure 11. HOCIGs, which are transformed into ADCIGs in Figure 12. The maximum subsurface offset is 0.8 km with an offset increment of 10 m. The low-wavenumber artifacts are evident at shallow depths of last two HOCIGs. The horizontal range of the ADCIGs coincides with the green box in Figure 2.

in the area of event overlap by DVB is a kind of average of the directions of the two (or more) plane waves. On the other hand, the LPWD methods consider overlapping events as the superimposed amplitudes of the different local plane waves propagating in different directions and so can be identified (Figure 6b and 6c), and potentially can accurately calculate the propagation angles and the corresponding amplitudes, as in the upper panels of Figure 13c or 13e, where events 1 and 2 are located at their corresponding reflection angles.

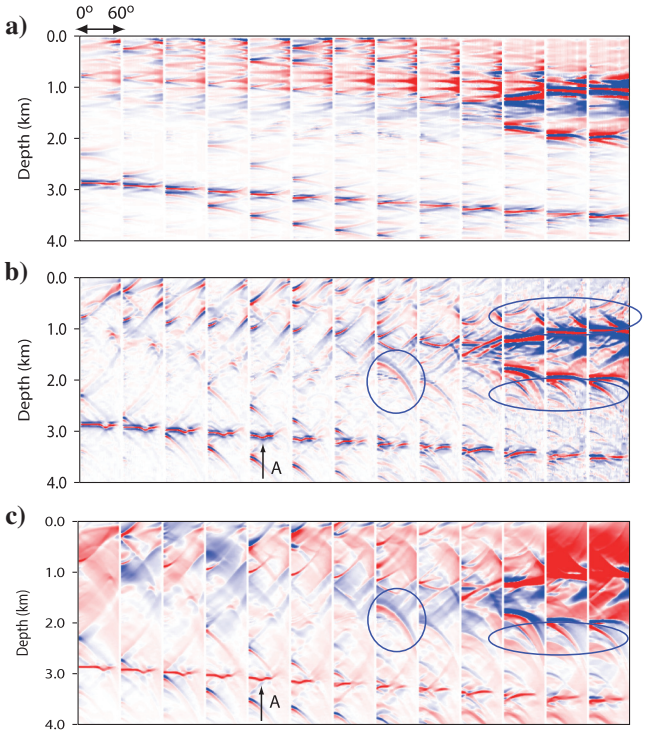

Figure 12. ADCIGs obtained from the LSIC method with FT obtained (a) using a small local window size of 32 × 32 grid points, and (b) by transforming each HOCIG. (c) shows the ADCIGs obtained by the LSIC method with SS transform. The horizontal ranges of the ADCIGs coincide with the green box in Figure 2. The event A is explained in Figure 13. The events in the blue ovals are smearing-effect artifacts. The low-wavenumber artifacts in (c) are from the those in Figure 11.

The ADCIGs obtained from the LPWD and the LSIC methods by transforming over small local windows (Figures 10a, 12a, 13b, and 13d) are very clean, and are without the smearing-effect artifacts because the small windows give a better approximation of the plane

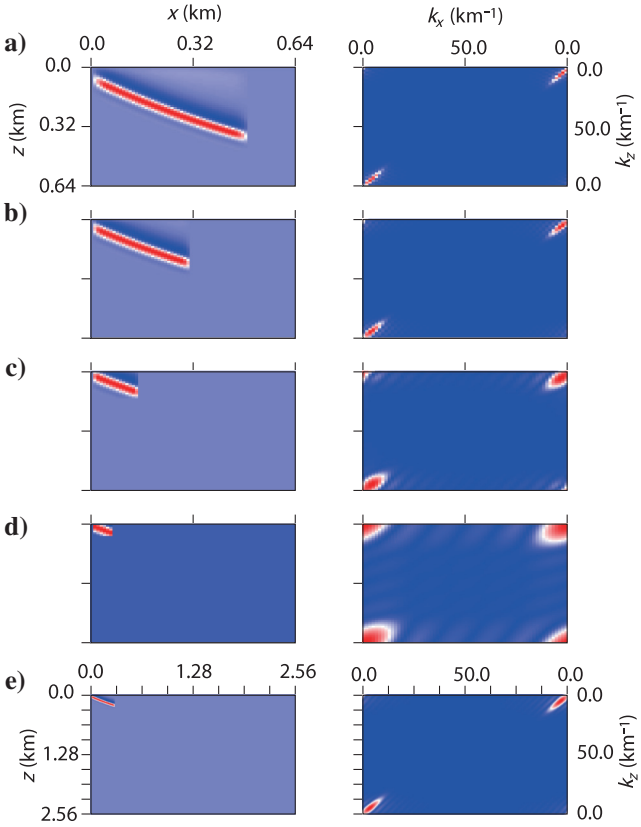

Figure 14. The left panels show the local plane waves in the (x, z) domain that are selected from the source wavefield (Figure 3) by the local small windows. The right panels show the corresponding wavefields in the (k_x, k_z) domain. The physical unit is km in the left panels, and km^{-1} in the right panels. In all the panels, 0.64 km contains 64 grid points. Angle resolution, which is determined from the range of wavenumbers, decreases with the decreasing window size before padding (a-d). Zero-padding does not change the angle resolution, but increases the number of wavenumber samples — compare (b) to (e).

Figure 13. ADCIG contributions for a single source (at 5.0-km horizontal position in Figure 2) for the two horizontal locations of the two black vertical lines (at horizontal position of 2.6 km (in the top rows) and 3.3 km (in the bottom rows)) shown in Figure 4, (a) is obtained by the amplitude-gradient method (equation 5), (b) by the LPWD method with window size of 32 × 32 grid points and (c) with the whole source and receiver wavefields (equations 18 and 19); (d) is obtained by the LSIC method with window size of 32 × 32 grid points and (e) with whole HOCIG (equation 20). The events 1 and 2 are the same reflection points illuminated at different reflection angles (see Figure 4), and the events 3 and 4 correspond to the events 3 and 4 of Figure 4. The event 3 introduces the concave artifact labeled A in Figures 7a, 7b, 10b, 12b, and 12c.

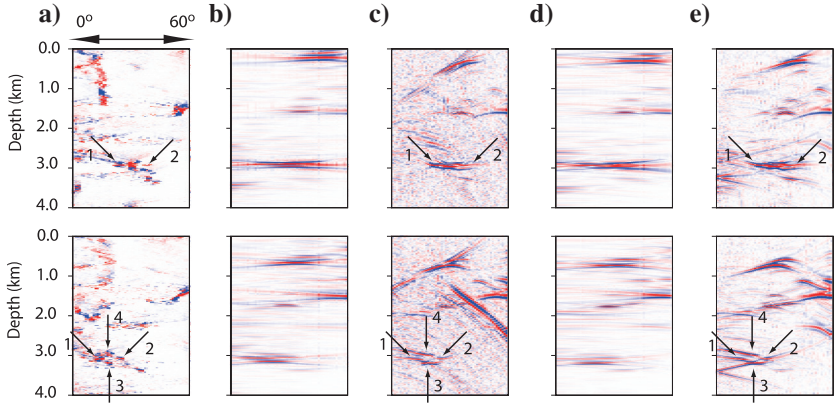

waves. However, the angle resolution of the ADCIGs are poor (Figures 10a, 12a, 13b, and 13d) by transforming the local wavefields in small local windows. The smaller the window, the poorer the angle resolution of the ADCIG (Figure 14). The DVB methods produce the highest-angle resolution (see the events labeled 1, 2, 3, and 4 in Figure 13a). The ADCIGs obtained from DVB methods have sharp terminations at far angles (e.g., see the terminations at points labeled B in Figure 7a–7d).

The ADCIGs obtained from the DVB, LPWD, and LSIC methods (by transforming the whole wavefields in LPWD, or the HOCIGs in LSIC) are very similar, with high angle resolutions. However, the LPWD and LSIC methods produce more noise, including serious smearing-effect artifacts, especially around the target (the blue ovals in Figures 10b and 12b) that result from transforming nonplanar waves, which do not satisfy the local-plane-wave assumptions. For these situations, the ADCIGs are not flat, even when the velocity model is correct. These artifacts are often curved up or down, and become stronger where velocity contrasts are larger or where sharp structure changes occur, such as at the edges of the circular target in Figure 2.

The LPWD and the LSIC methods produce very similar ADCIGs because both are based on the local-plane-wave assumptions. In both methods, the ADCIG quality and angle resolution depend on the window size, and both methods have been implemented by either an FT or an SS transform. The ADCIGs obtained by SS have a phase-shifted waveform (Figure 12c) (Phinney et al., 1981; Durrani and Bisset, 1984; Tatham, 1984), whereas the ADCIGs by FT (Figure 12a or 12b) do not (Luo et al., 2010) because they are taken at the zero-offset of the HOCIGs (the zero-lag cross-correlation of the source and receiver wavefields) after calculating the reflection angles in the frequency/wavenumber domain.

The LPWD and the LSIC methods are implemented in different ways. The LPWD method uses the most energetic wavenumber either by setting a threshold of the minimum energy of a wavenumber in the whole wavefield in the frequency/wavenumber domain, or by the ALFT in small local windows (Xu et al., 2011), whereas the LSIC method uses all wavenumbers. Thus, the computation times of the two methods are also different. The LSIC method is much faster than the LWPD method because the 2D FT and the wavenumber-to-reflection angle conversions (equation 25) are done only

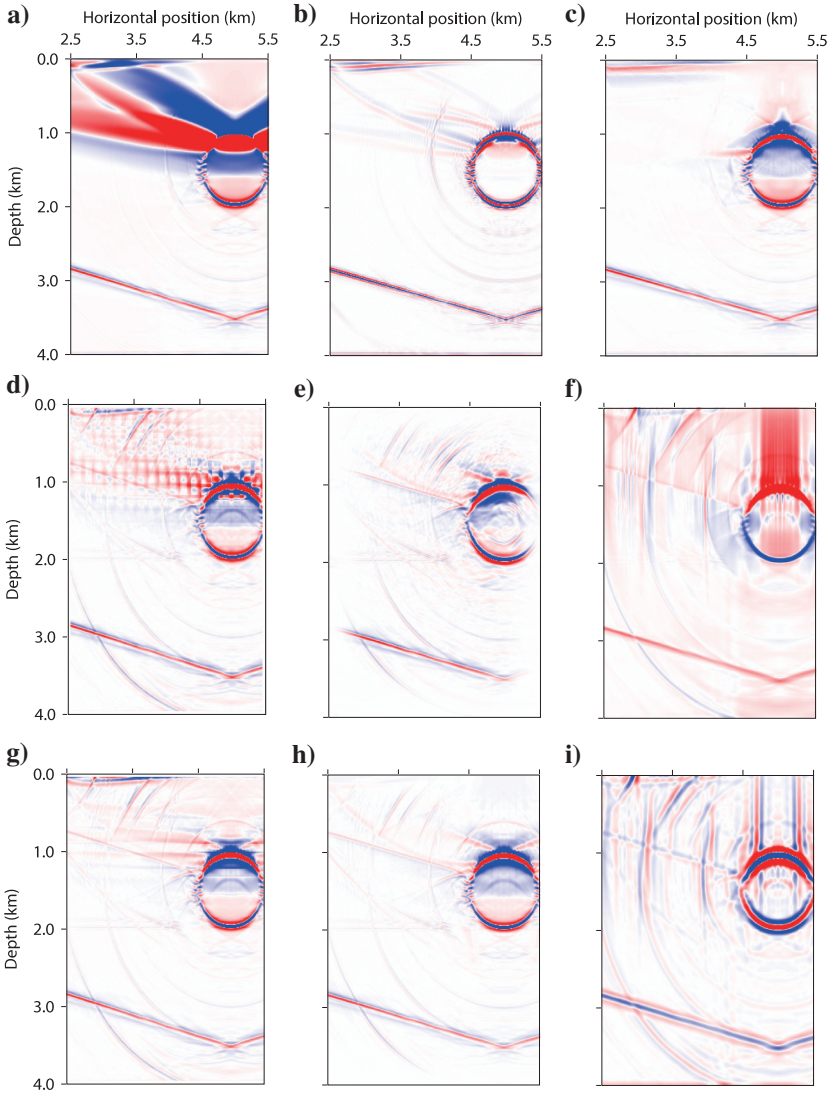

Figure 15. (a) The direct stacked image of prestack migrated shot gathers, not ADCIGs, and (b) the image obtained by applying a Laplace filter to (a). Panels (c-h) are stacked images from ADCIGs using reflection angles of 0° to 60°, obtained by (c) amplitude-gradient method, LPWD (FT) method with (d) local windows and with (e) whole wavefield, (f) LISC (SS) method, LSIC (FT) method with (g) local windows and with (h) each HOCIG, respectively. Panel (i) is the image obtained by applying a Laplacian filter to (f). The boundary of the images coincide with the green box in Figure 2.

once for each HOCIG in the LSIC method (Luo et al., 2010), whereas for the LWPD, 2D FTs, wavenumber-domain convolution (equation 18), and wavenumber-to-propagation angle conversions (equation 17) are performed iteratively in frequency and source loops (Xu et al., 2011). For 3D data, the LSIC computation will be very expensive because they require 5D FTs to ODCIGs and a correponding mapping between reflection angles and wavenumbers (Fomel, 2004; Xu et al., 2011).

If the ADCIGs are stacked over reflection angles from 0° to 60° in the present example, we get a stacked image that is free of the low-wavenumber artifacts (Figure 15c, 15d, 15e, 15g, and 15h). The stacked image obtained from the amplitude-gradient method (a DVB) is cleaner than that from LPWD method with the local windows (compare Figure 15c and 15d) and is more complete in the subtarget area than the LPWD method, by transforming whole source and receiver wavefields (compare Figure 15c and 15e). The stacked image obtained by the LSIC method (FT) is similar to that from LPWD method (FT) because the ADCIGs from both methods are very similar (compare Figure 15d and 15e, and 15g and 15h).

The low-wavenumber artifacts in the stacked image can also be removed by a Laplace filter (Zhang and Sun, 2009) with less computation time (Figure 15b), but this alters the phase of the image (compare the images in Figure 15a and 15b). Therefore, if the purpose is to look at angle dependence of amplitude or phase (Zhu and McMechan, 2012), then the Laplace filter, or any other filter that alters the phase should not be applied, or these effects should be corrected (Zhang and Sun, 2009).

All of the three main methods calculate phase propagation angles, which are perpendicular to the local plane waves. So all of them can be directly applied to calculate angle gathers in isotropic and anisotropic media if angle gathers are binned according to the phase propagation angles.

Table 1 contains comparison of the cost and performance of all the methods on the bases of computation time, memory, and disk space requirements. The comparison of computation time of methods that use the time domain and the frequency domain crosscorrelation start from reading the snapshots in the time domain or the frequency domain, and do not include the extrapolation time and time-to-frequency 1D Fourier transformation.

Comparison of the computation time between the LPWD method, with local windows and with the whole wavefield, is approximate because different algorithms are used to extract the most energetic wavenumbers. The LPWD method with the local window can be made faster and more efficient; refer to Xu et al. (2011) for the details of the algorithm and computation time.

The computation times for the DVB method using the two highest amplitude arrivals are given as a range in Table 1 because the time depends on the number of processors used per node, because of the I/O bottleneck when reading snapshots at all time steps, and because of the additional CPU time needed to extract and sort a few highest-amplitude arrivals compared to selecting only the highest one. I/O time can be faster with a higher network bandwidth using higher performance disks. The I/O bottleneck may also be reduced by using the various source wavefield reconstruction algorithms (Nguyen and McMechan, 2009), check pointing (Symes, 2007), or the method based on the random boundary condition (Fei and Williamson, 2010). The computation time may increase a little when more arrivals are included, but the increase is small compared to the I/O time.

In elastic media, propagation directions can be computed directly from the x-, y-, and z-component amplitudes of the P- and S-waves if they are well preserved after separation (Zhang and McMechan, 2010), or if P- and S-waves are extrapolated separately (Ma and Zhu, 2003), or computed directly from stress and particle velocity components (Dickens and Winbow, 2011) using the elastodynamic equations (Virieux, 1984, 1986), so the cost is minimal.

Amplitudes are not explicitly, quantitatively, considered above, but would be needed for true-amplitude RTM for subsequent application of AVA analysis. The comparisons of all the ADCIG methods above provide a reference for choosing an appropriate method for

Table 1. Comparison of the computation time, memory requirement, and disk space requirements in this example (Figure 2). The computation time to process one shot into its ADCIG contributions is measured on a 2.93 GHz Intel Xeon X5670 processor. "All" means the full wavefields, and "two highest" means the two highest amplitudes, which are picked by scanning the wavefield over all time steps at each grid point. "Amplitude" is the amplitude-gradient method, and "phase" is the phase-gradient method. "S" means the source propagation angles, "R" means the receiver propagation angles, and "D" means the reflector dip angles.

	Computation time (for one shot)	Memory requirement (byte)	Disk space requirement (byte)
All, amplitude, S & R	15.0 min	115.2 M	$2*]N_xN_zN_t/8=]$2.4 G
All, phase, S & R	115.0 min	115.2 M	$2*]N_xN_zN_t/8=]$2.4 G
All, amplitude, S & D	7.0 min	105.6 M	$2*]N_xN_zN_t/8=]$2.4 G
All, phase, S & D	56.0 min	105.6 M	$2*]N_xN_zN_t/8=]$2.4 G
Two highest, amplitude, S & D	19.5 min — 105.0 min	28.8 M	$2*]N_xN_zN_t=]$19.2 G
Two highest, phase, S & D	21.5 min — 106.5 min	28.8 M	$2*]N_xN_zN_t=]$19.2 G
LPWD (window)	18.0 hours	3.5 G	$2*]N_xN_zN_t/8=]$2.4 G
LPWD (whole)	55.7 min	4.3 G	$2*]N_xN_zN_t/8=]$2.4 G
LSIC (window) [+FT]	2.8 min [+0.63 min /CIG]	250 M (time domain) 3.8 G (frequency domain)	$2*]N_xN_zN_t/8=]$2.4 G
LSIC (whole) [+FT]	2.8 min [+0.16 min /CIG]	250 M (time domain) 3.8 G (frequency domain)	$2*]N_xN_zN_t/8=]$2.4 G

further applications of wave-equation MVA, and provide a reference for future studies of true amplitude ADCIGs.

CONCLUSIONS

Eleven methods for extracting ADCIGs from RTM, including a new DVB method using the instantaneous phase, are compared. The DVB methods can be implemented, using either amplitude or instantaneous phase gradients; both give virtually undistinguishable results.

None of the DVB methods can separate overlapping events, so the angle calculation are less reliable where there are overlapping events, whereas the LPWD and LSIC methods can, and also potentially can preserve the amplitudes. The LPWD methods and the LSIC methods produce almost the same ADCIGs. The results of both depend on the window size used. When using a small window, the ADCIGs are clean, but the angle resolution is lower. When using a large window, the angle resolution is higher but the ADCIGs are noisier and include smearing-effect artifacts when the data do not satisfy the local-plane-wave assumptions.

ACKNOWLEDGMENTS

The research leading to this paper was supported by the Sponsors of the UT-Dallas Geophysical Consortium. We thank the Texas Advanced Computing Center for providing high performance computing time. J.H. thanks Total E&P for an internship, and Rui Yan for helpful discussions and information. We thank Paul Williamson, Mauricio Sacchi, Faqi Liu, and three anonymous reviewers for helpful comments. This paper is Contribution No. 1256 from the Geosciences Department at the University of Texas at Dallas.

APPENDIX A

INSTANTANEOUS PHASE GRADIENTS

Figure A-1a shows a 2D wavefield snapshot propagating in an isotropic constant velocity model, from a source at the center of the model. Taking 1D Hilbert transforms of this 2D wavefield over the horizontal and vertical directions gives $\nabla\varphi_1(x,z)]$(Figure A-1b) and $\nabla\varphi_2(x,z)]$(Figure A-1d), respectively. As detailed by Havlicek et al. (1998), the phase gradient directions are opposite to the propagation directions in quadrants II and III for $\nabla\varphi_1$ (from the horizontal Hilbert transform) (Figure A-1b), and in quadrants I and II for $\nabla\varphi_2$ (from the vertical Hilbert transform) (Figure A-1d).

To get the correct propagation directions in all quadrants, we multiply the spatial derivatives of the phase by the first time derivative of the phase (obtained by taking the difference in phase from a second wavefield snapshot at an adjacent time step). Figures A-1c and A-1e are $\nabla\varphi_1 \cdot \frac{\partial\varphi_1}{\partial t}$ and $\nabla\varphi_2 \cdot \frac{\partial\varphi_2}{\partial t}$, respectively; both give the same (correct) propagation directions of the 2D wavefield. This example demonstrates the conclusion of Havlicek et al. (1998) that 1D directional Hilbert transforms of a 2D wavefield (or image) over the horizontal and vertical directions are functionally equivalent, and with the appropriate modification, either can be used to calculate the instantaneous phase and the instantaneous phase gradient of the 2D data.

For 3D data, the 1D direction Hilbert transform over the horizontal directions x, y, and over the depth z give $\mathbf{q}_1(x,y,z)$, $\mathbf{q}_2(x,y,z)$, and $\mathbf{q}_3(x,y,z)$, from which $\varphi_1(x,y,z)$, $\varphi_2(x,y,z)$, and $\varphi_3(x,y,z)]$

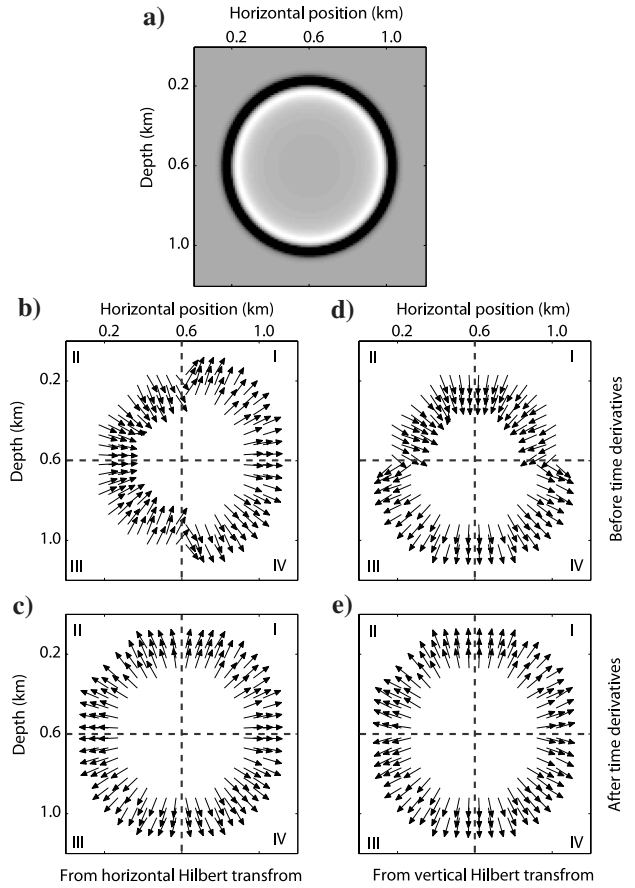

Figure A-1. (a) Synthetic 2D wavefield snapshot. (b) and (d) are $\nabla\varphi_1$ and $\nabla\varphi_2$ respectively (equation 10). (c) and (e) are $\nabla\varphi_1 \cdot \frac{\partial\varphi_1}{\partial t}$ and $\nabla\varphi_2 \cdot \frac{\partial\varphi_2}{\partial t}$ respectively after multiplying by the time derivative of the phases (equation 11). (b) and (c) are the phase gradients obtained by 1D horizontal Hilbert transformation of (a); (d) and (e) are the phase gradients obtained by 1D vertical Hilbert transformation of (a). A median filter is applied to the computed propagation directions in (b-e).

are obtained. The propagation direction in 3D is then obtained from the instantaneous phase using

$$\nabla\varphi(x,y,z)]\cdot\frac{\partial\varphi}{\partial t} =]\ \frac{\partial\varphi}{\partial x},\frac{\partial\varphi}{\partial y},\frac{\partial\varphi}{\partial z}\ \cdot\frac{\partial\varphi}{\partial t}, \tag{A-1}$$

which is similar to the Poynting vector based method for 3D data (Vyas et al., 2011b; Yoon et al., 2011; Yan and Ross, 2013),

$$\nabla\mathbf{U}(x,y,z)]\cdot\frac{\partial\mathbf{U}}{\partial t} =]\ \frac{\partial\mathbf{U}}{\partial x},\frac{\partial\mathbf{U}}{\partial y},\frac{\partial\mathbf{U}}{\partial z}\ \cdot\frac{\partial\mathbf{U}}{\partial t}. \tag{A-2}$$

REFERENCES

Baysal, E., D. Kosloff, and J. W. C. Sherwood, 1984, A two-way nonreflecting wave equation: Geophysics, **49**, 132–141, doi: 10.1190/1.1441644.
Biondi, B., and G. Palacharla, 1996, 3-D prestack migration of common-azimuth data: Geophysics, **61**, 1822–1832, doi: 10.1190/1.1801945.

Biondi, B., and W. W. Symes, 2004, Angle-domain common-image gathers for migration velocity analysis by wavefield-continuation imaging: Geophysics, **69**, 1283–1298, doi: 10.1190/1.1801945.
Chang, W. F., and G. A. McMechan, 1990, 3D acoustic prestack reverse-time migration: Geophysical Prospecting, **38**, 737–755, doi: 10.1111/j1365-2478.1990tb01872.x.
Chang, W. F., and G. A. McMechan, 1986, Reverse-time migration of set vertical seismic profiling data using the excitation-time imaging condition: Geophysics, **51**, no. 3, 67–84.
Chattopadhyay, S., and G. A. McMechan, 2008, Imaging conditions for prestack reversetime migration: Geophysics, **73**, no. 3, S81–S89, doi: 10.1190/1.2903822.
Dickens, A., and G. A. Winbow, 2011, RTM angle gathers using Poynting vectors: 81st Annual International Meeting, SEG, Expanded Abstracts, 3109–3113.
Durrani, T. S., and D. Bisset, 1984, The Radon transform and its properties: Geophysics, **49**, 1180–1187, doi: 10.1190/1.1441747.
Fei, W., and P. Williamson, 2010, Overcoming the I/O bottleneck of adjoint state method based migration velocity analysis: 80th Annual International Meeting, SEG, Expanded Abstracts, 4057–4061.
Fomel, S., 2004, Theory of 3-D angle gathers in wave-equation imaging: 74th Annual International Meeting, SEG, Expanded Abstracts, 1053–1056.
French, W. S., 1974, Two-dimensional and three-dimensional migration of model experiment reflection profiles: Geophysics, **39**, 265–277, doi: 10.1190/1.1440426.
Gardner, G. H. F., W. S. French, and T. Matzuk, 1974, Elements of migration and velocity analysis: Geophysics, **39**, 811–825, doi: 10.1190/1.1440468.
Gray, S. H., 2005, Gaussian beam migration of common-shot records: Geophysics, **70**, no. 4, S71–S77, doi: 10.1190/1.1988186.
Havlicek, J. P., J. W. Havlicek, N. D. Mamuya, and A. C. Bovik, 1998, Skewed 2D Hilbert transforms and computed AM-FM models: Proceedings of the IEEE International Conference on Image Processing, 602–606.
Hill, N. R., 2001, Prestack gaussian-beam depth migration: Geophysics, **66**, 1240–1250, doi: 10.1190/1.1487071.
Kaelin, B., and A. Guitton, 2006, Imaging condition for reverse time migration: 76th Annual International Meeting, SEG, Expanded Abstracts, 4–2598.
Liu, F., G. Zhang, S. Morton, and J. Leveille, 2007, Reverse-time migration using one-way wavefield imaging condition: 77th Annual International Meeting, SEG, Expanded Abstracts, 2170–2174.
Liu, J., and W. Han, 2010, Automatic event picking and tomography on 3D RTM angle gather: 80th Annual International Meeting, SEG, Expanded Abstracts, 4263–4267.
Luo, M., R. Lu, G. Winbow, and L. Bear, 2010, A comparison of methods for obtaining local image gathers in depth migration: 80th Annual International Meeting, SEG, Expanded Abstracts, **324**, 7–3251.
Ma, D., and G. Zhu, 2003, P- and S-wave separated elastic wave equation numerical modeling (in Chinese): Geophysical Prospecting, **38**, 482–486.
Mulder, W. A., and R. E. Plessix, 2003, One-way and two-way wave equation migration: 73rd Annual International Meeting, SEG, Expanded Abstracts, 881–884.
Nguyen, B., and G. A. McMechan, 2009, Comparative evaluation of options for source wavefield reconstruction in reverse-time migration: Journal of Seismic Exploration, **18**, 305–314.
Nolan, C. J., and W. W. Symes, 1996, Imaging and coherency in complex structures: 66th Annual International Meeting, SEG, Expanded Abstracts, 759–362.
Ottolini, R., 1982, Migration of reflection seismic data in angle-midpoint coordinates: Ph.D. thesis, Standford University.
Panizzardi, J., N. Bienati, and E. Gentile, 2011, Non hyperbolic moveout anisotropic MVA: 81st Annual International Meeting, SEG, Expanded Abstracts, 3913–3917.
Patrikeeva, N., and P. Sava, 2013, Comparison of angle decomposition methods for waveequation migration: 83rd Annual International Meeting, SEG, Expanded Abstracts, 3773–3778.
Phinney, R. A., K. R. Chowdhury, and L. N. Frazer, 1981, Transformation and analysis of record sections: Journal of Geophysical Research Solid Earth : JGR, **86**, no. B1, 359–377, doi: 10.1029/JB086iB01p00359.
Pratt, R. R., 1990, Frequency-domain elastic wave modeling by finite differences: A tool for crosshole seismic imaging: Geophysics, **55**, 626–632, doi: 10.1190/1.1442874.
Sava, P., and B. Biondi, 2004, Wave-equation migration velocity analysis: Geophysical Prospecting, **52**, 593–606, doi: 10.1111/j.1365-2478.2004.00447.x.
Sava, P., and S. Fomel, 2003, Angle-domain common-image gathers by wavefield continuation methods: Geophysics, **68**, 1065–1074, doi: 10.1190/1.1581078.
Sava, P., and S. Fomel, 2005a, Coordinate-independent angle-gathers for wave equation migration: 75th Annual International Meeting, SEG, Expanded Abstracts, 2052–2055.
Sava, P., and S. Fomel, 2005b, Wave equation common-angle gathers for converted wave: 75th Annual International Meeting, SEG, Expanded Abstracts, 947–951.
Sava, P., and S. Fomel, 2006a, Time-shift imaging condition for converted waves: 76th Annual International Meeting, SEG, Expanded Abstracts, 2460–2464.
Sava, P., and S. Fomel, 2006b, Time-shift imaging condition in seismic migration: Geophysics, **71**, no. 6, S209–S217, doi: 10.1190/1.2338824.
Sava, P., and L. Vlad, 2008, Numeric implementation of wave-equation migration velocity analysis operators: Geophysics, **73**, no. 5, VE145–VE159, doi: 10.1190/1.2953337.
Schneider, W. A., 1978, Integral formulation for migration in two and three dimensions: Geophysics, **43**, 49–76, doi: 10.1190/1.1440828.
Shan, G., and B. Biondi, 2008, Angle-domain common-image gathers for steep reflectors: 78th Annual International Meeting, SEG, Expanded Abstracts, 3068–3072.
Shen, P., and W. W. Symes, 2008, Automatic velocity analysis via shot profile migration: Geophysics, **73**, no. 5, VE49–VE59, doi: 10.1190/1.2972021.
Siliqi, R., P. Jerrmann, A. Prescott, and L. Capar, 2007, High order RMO picking using uncorrelated parameters: 77th Annual International Meeting, SEG, Expanded Abstracts, 2772–2776.
Siliqi, R., and A. Talaalout, 2009, Structurally coherent wide azimuth residual moveout surfaces: 79th Annual International Meeting, SEG, Expanded Abstracts, **403**, 9–4043.
Sun, W., and L. Fu, 2013, Two effective approaches to reduce data storage in reverse time migration: Computers & Geosciences, **56**, 69–75, doi: 10.1016/j.cageo.2013.03.013.
Symes, W. M., 2007, Reverse time migration with optimal checkpointing: Geophysics, **72**, no. 5, SM213–SM221, doi: 10.1190/1.2742686.
Tatham, R. H., 1984, Multidimensional filtering of seismic data: Proceedings of the IEEE, **72**, 1357–1369, doi: 10.1109/PROC.1984.13023.
Virieux, J., 1984, SH-wave propagation in heterogeneous media: Velocity-stress finite-difference method: Geophysics, **49**, 1933–1942, doi: 10.1190/1.1441605.
Virieux, J., 1986, P-SV wave propagation in heterogeneous media: Velocity-stress finite-difference method: Geophysics, **51**, 889–901, doi: 10.1190/1.1442147.
Vyas, M., X. Du, E. Mobley, and R. Fletcher, 2011a, Methods for computing angle gathers using RTM: 73rd Conference and Exhibition, EAGE, Expanded Abstracts, F020.
Vyas, M., D. Nichols, and E. Mobley, 2011b, Efficient RTM angle gathers using source directions: 81st Annual International Meeting, SEG, Expanded Abstracts, 3104–3108.
Whitmore, D., and L. R. Lines, 1986, Vertical seismic profiling data using the excitation-time imaging condition: Geophysics, **51**, no. 1, 67–84.
Xie, X., and R. S. Wu, 2002, Extracting angle domain information from migrated wavefields: 72nd Annual International Meeting, SEG, Expanded Abstracts, 1360–1363.
Xie, X., and H. Yang, 2008a, A full-wave equation based seismic illumination analysis method: 70th Annual International Conference and Exhibition, EAGE, Extended Abstracts, P284.
Xie, X., and H. Yang, 2008b, The finite-frequency sensitivity kernel for migration residual moveout and its applications in migration velocity analysis: Geophysics, **73**, no. 6, S241–S249, doi: 10.1190/1.2993536.
Xu, S., H. Chauris, G. Lambaré, and M. Noble, 2001, Common-angle migration: A strategy for imaging complex media: Geophysics, **66**, 1877–1894, doi: 10.1190/1.1487131.
Xu, K., B. Zhou, and G. A. McMechan, 2010a, Implementation of prestack reverse-time migration using frequency-domain extrapolation: Geophysics, **75**, no. 2, S61–S72, doi: 10.1190/1.3339386.
Xu, S., Y. Zhang, and G. Lambaré, 2010b, Antileakage Fourier transform for seismic data regularization in higher dimension: Geophysics, **75**, no. 6, WB113–WB120, doi: 10.1190/1.3507248.
Xu, S., Y. Zhang, D. Pham, and G. Lambaré, 2005, Antileakage Fourier transform for seismic data regularization: Geophysics, **70**, no. 6, Z87–Z93, doi: 10.1190/1.2146080.
Xu, S., Y. Zhang, and B. Tang, 2011, 3D angle gathers from reverse time migration: Geophysics, **76**, no. 2, S77–S92, doi: 10.1190/1.3536527.
Yan, J., and W. Ross, 2013, Improving the stability of angle gather computation using Poynting vectors: 83rd Annual International Meeting, SEG, Expanded Abstracts, 3784–3788.
Yan, J., and P. Sava, 2008, Isotropic angle-domain elastic reverse-time migration: Geophysics, **73**, no. 6, S229–S239, doi: 10.1190/1.2981241.
Yan, R., and X. Xie, 2009, A new angle-domain imaging condition for reverse time migration: 79th Annual International Meeting, SEG, Expanded Abstracts, 2784–2788.
Yan, R., and X. Xie, 2010, A new angle-domain imaging condition for elastic reverse time migration: 80th Annual International Meeting, SEG, Expanded Abstracts, 3181–3186.
Yan, R., and X. Xie, 2011, Angle gather extraction for acoustic and isotropic elastic RTM: 81st Annual International Meeting, SEG, Expanded Abstracts, 3141–3146.

Yan, R., and X. Xie, 2012, An angle-domain imaging condition for elastic reverse time migration and its application to angle gather extraction: Geophysics, **77**, no. 5, S105–S115, doi: 10.1190/geo2011-0455.1.

Yoon, K., M. Guo, J. Cai, and B. Wang, 2011, 3D RTM angle gathers from source wave propagation direction and dip of reflector: 81st Annual International Meeting, SEG, Expanded Abstracts, 1057–1060.

Yoon, K., K. Marfurt, and E. W. Starr, 2004, Challenges in reverse-time migration: 74th Annual International Meeting, SEG, Expanded Abstracts, 1057–1060.

Yoon, K., and K. J. Marfurt, 2006, Reverse-time migration using the Poynting vector: Exploration Geophysics, **37**, 102–107, doi: 10.1071/EG06102.

Zhang, Q., and G. A. McMechan, 2010, 2-D and 3-D elastic wavefield vector decomposition in the wavenumber domain for VTI media: Geophysics, **75**, no. 3, D13–D26, doi: 10.1190/1.3431045.

Zhang, Q., and G. A. McMechan, 2011a, Common-image gathers in the incident phase-angle domain from reverse time migration in 2D elastic VTI media: Geophysics, **76**, no. 6, S197–S206, doi: 10.1190/geo2011-0015.1.

Zhang, Q., and G. A. McMechan, 2011b, Direct vector-field method to obtain angle-domain common-image gathers from isotropic acoustic and elastic reverse-time migration: Geophysics, **76**, no. 5, WB135–WB149, doi: 10.1190/geo2010-0314.1.

Zhang, Y., and B. Biondi, 2013, Moveout-based wave-equation migration velocity analysis: Geophysics, **78**, no. 2, U31–U39, doi: 10.1190/geo2012-0082.1.

Zhang, Y., and J. Sun, 2009, Practical issues of reverse time migration: True-amplitude gathers, noise removal and harmonic-source encoding: First Break, 53–59.

Zhang, Y., S. Xu, B. Tang, B. Bai, Y. Huang, and T. Huang, 2010, Angle gathers from reverse time migration: The Leading Edge, **29**, 1364–1371, doi: 10.1190/1.3517308.

Zhang, Y., G. Zhang, and N. Bleistein, 2003, True amplitude wave equation migration arising from true amplitude one-way wave equations: Inverse Problems, **19**, 1113–1138, doi: 10.1088/0266-5611/19/5/307.

Zhu, X., and G. A. McMechan, 2012, Elastic inversion of seismic reflection data using phase variation with angle: Geophysics, **77**, no. 4, R149–R159, doi: 10.1190/geo2011-0230.1.